CALPHAD: Computer Coupling of Phase Diagrams and Thermochemistry 95 (2026) 103016

Contents lists available at ScienceDirect

Calphad

journal homepage: www.elsevier.com/locate/calphad

Experimental investigation of phase equilibria in the Cr-Mo-Si ternary system at 1500 °C

Arun Ramasamy Chitra *, Kateryna Khanchych, Bronislava Gorr

Institute of Applied Materials (IAM), Karlsruhe Institute of Technology (KIT), Kaiserstraße 12, Karlsruhe, 76131, Germany

ARTICLE INFO

Keywords:
Cr-Mo-Si
1500 °C
Phase equilibrium
σ-phase
Isothermal section

ABSTRACT

Phase equilibria in a Si-lean region ($x_{Si} \leq 25$ at.%) of the Cr-Mo-Si ternary system at 1500 °C is experimentally investigated by means of scanning electron microscopy (SEM) coupled with energy dispersive X-ray spectroscopy (EDX), electron probe microanalysis (EPMA) and X-ray diffraction (XRD). For the first time, the existence of a stable ternary compound (σ-phase) after the heat treatment at 1500 °C for 200 h is confirmed. The σ-phase is stable within 12.5-13.5 at.% of silicon, 30.6-48.3 at.% of molybdenum and 38.7-56.8 at. % of chromium. The partial isothermal section at 1500 °C refined in the vicinity of the σ-phase is constructed based on newly obtained experimental data. The examined section contains three single-phase regions ($(Cr,Mo)_3Si$, σ-phase and a single-phase solid solution (Cr,Mo)ss), three two-phase regions ((Cr,Mo)ss + $(Cr,Mo)_3Si$, σ + (Cr,Mo)ss and σ + $(Cr,Mo)_3Si$), and one three-phase region (σ + (Cr,Mo)ss + $(Cr,Mo)_3Si$).

1. Introduction

Alloys containing significant portion of refractory metals such as tungsten, niobium, tantalum, and molybdenum have been considered for decades as perspective candidates for operation under extreme conditions including very high temperatures typically above ~1100 °C, mechanical loads and aggressive environments [1,2]. Classical aforementioned refractory metals possess body centered cubic (BCC) crystal structure and melting points above 2000 °C. Some textbooks classify also chromium and rhenium as refractory metals. The intrinsic high melting points of refractory metals create a significant temperature margin above the state-of-the-art nickel alloys, potentially opening opportunities for improved thermodynamic efficiency of high temperature technologies such as gas turbine, thermal energy storage systems and concentrated solar power [3,4]. A key advantage is their superior mechanical properties, particularly their high elastic modulus, creep resistance, and strength retention above 1000 °C. For example, W has excellent high-temperature strength and low creep rates, whereas Mo provides a good balance of strength and density [5,6]. However, these materials present significant disadvantages, including poor room-temperature ductility in BCC alloys structures), susceptibility to brittle fracture, high density (notably W and Re), and difficulties in fabrication and machining due to their hardness and brittleness [5,7]. Moreover, traditional refractory systems have inadequate oxidation resistance, as many form fast growing (Ta_2O_5, Nb_2O_5 [8–10]) or volatile oxides (MoO_3 or Re_2O_7 [11,12]), which restricts their practical use to environments with low oxygen activities [13].

Considering oxidation resistance, chromium-based alloys possess an essential advantage due to chromium's ability to form stable and protective oxide scales such as Cr_2O_3 at temperatures below 1050 °C [14]. Additionally, Cr-based alloys provide a good combination of properties, combining a relatively low density with the ability to tailor mechanical performance through alloying additions (e.g., Nb, Ti, Mo, Si) [13,15]. Despite these advantages, significant challenges remain that limit the widespread use of Cr-based refractory alloys. One of the most important difficulties is their intrinsic brittleness, especially at low temperatures, which is related to a high ductile-to-brittle transition temperature (DBTT) in the range of 500 °C-700 °C [15] and the occurrence of brittle intermetallic phases such as Laves phases [16]. Although oxidation resistance is superior relative to other refractory metals, degradation mechanisms such as oxide volatilization, nitridation and environmental embrittlement still occur at elevated temperatures [16].

Recent investigations by Hinrichs et al., [11] reported that the (Cr, Mo)ss phase in the Cr-36.1Mo-3Si (at.%) alloy exhibits significant room-temperature ductility and resistance to both oxidation and nitridation up to 1200 °C. In Cr-Mo-Si alloys, molybdenum contributes to a high melting point and mechanical strength at temperatures above 1100 °C, forming a BCC load-bearing matrix. As mentioned earlier,

* Corresponding author.
E-mail address: arun.chitra@kit.edu (A. Ramasamy Chitra).

https://doi.org/10.1016/j.calphad.2026.103016
Received 28 April 2026; Received in revised form 7 October 2026; Accepted 18 October 2026
Available online 20 October 2026
0364-5916/© 2026 The Authors. Published by Elsevier Ltd. This is an open access article under the CC BY license (http://creativecommons.org/licenses/by/4.0/).
Open access funding enabled and organized by Projekt DEAL.

chromium allows the formation of a protective Cr_2O_3 scale that serves as the primary barrier against oxidation, whereas a modest Si addition generates a thin SiO_2 layer at the oxide/metal interface suppressing the volatilization of MoO_3 and markedly improving resistance to nitridation [11,17,18].

However, the information regarding phase equilibria in this ternary system is incomplete and controversial. The most comprehensive review of the existing experimental data for the Cr-Mo-Si system was performed by Pandelaers and Schmid-Fetzer [19]. Currently, the existence of two ternary phases is established – a σ-phase with approximate composition $Cr_{43}Mo_{43}Si_{14}$ [20] and a poorly investigated $Cr_{47}Mo_9Si_{44}$ [21] phase (in at.%). There is no available information whether the σ-phase is formed from the liquid or solid phases. The second ternary phase with a composition around $Cr_{47}Mo_9Si_{44}$ was observed by Svechnikov et al., [21] at 1300 °C, however, its crystal structure was not studied. Three isothermal sections at 1000, 1200 and 1300 °C as well as liquidus surface have been reported [21,22]. The lack of data in the ternary system at higher temperatures, inconsistencies regarding multi-phase fields in the mentioned reports and equilibrium compositions of the ternary phases, in particular the σ-phase, hinder the development of this alloy system for practical application.

The present work experimentally investigates phase equilibria in the Si-lean alloy series ($x_{Si} \leq 25$ at.%) of the Cr-Mo-Si system at 1500 °C. The proposed partial isothermal section provides a significantly improved understanding of the multi-phase fields in the vicinity of the σ-phase as well as its equilibrium composition and provides a foundation for revising the existing thermodynamic description of the Cr–Mo–Si system reported in Ref. [23]. The review of the corresponding binary and ternary systems will be presented below.

2. Literature review

2.1. Cr-Si system

The Cr-Si binary phase diagram was first proposed by Kieffer [24]. It based on extensive experimental data suggesting that along with terminal solid solutions it contains four stoichiometric compounds: Cr_3Si, Cr_2Si, Cr_3Si_2 and $CrSi_2$. Subsequent investigations [25–27] by means of microstructural analysis, XRD and differential thermal analysis (DTA) have refined a stoichiometry of the Cr_3Si_2 and Cr_2Si phases identifying CrSi and Cr_5Si_3 instead. An additional high-temperature β - Cr_5Si_3 phase was first reported at 1505 °C based on DTA measurements [26]. Du and Schuster [28] have refined the CrSi-Si partial system within the composition range $45 \leq x_{Si} \leq 100$ at. % and significantly corrected the most invariant reaction temperatures employing DTA and XRD. Most recently, Ioroi et al. [29] have updated the entire Cr-Si system between

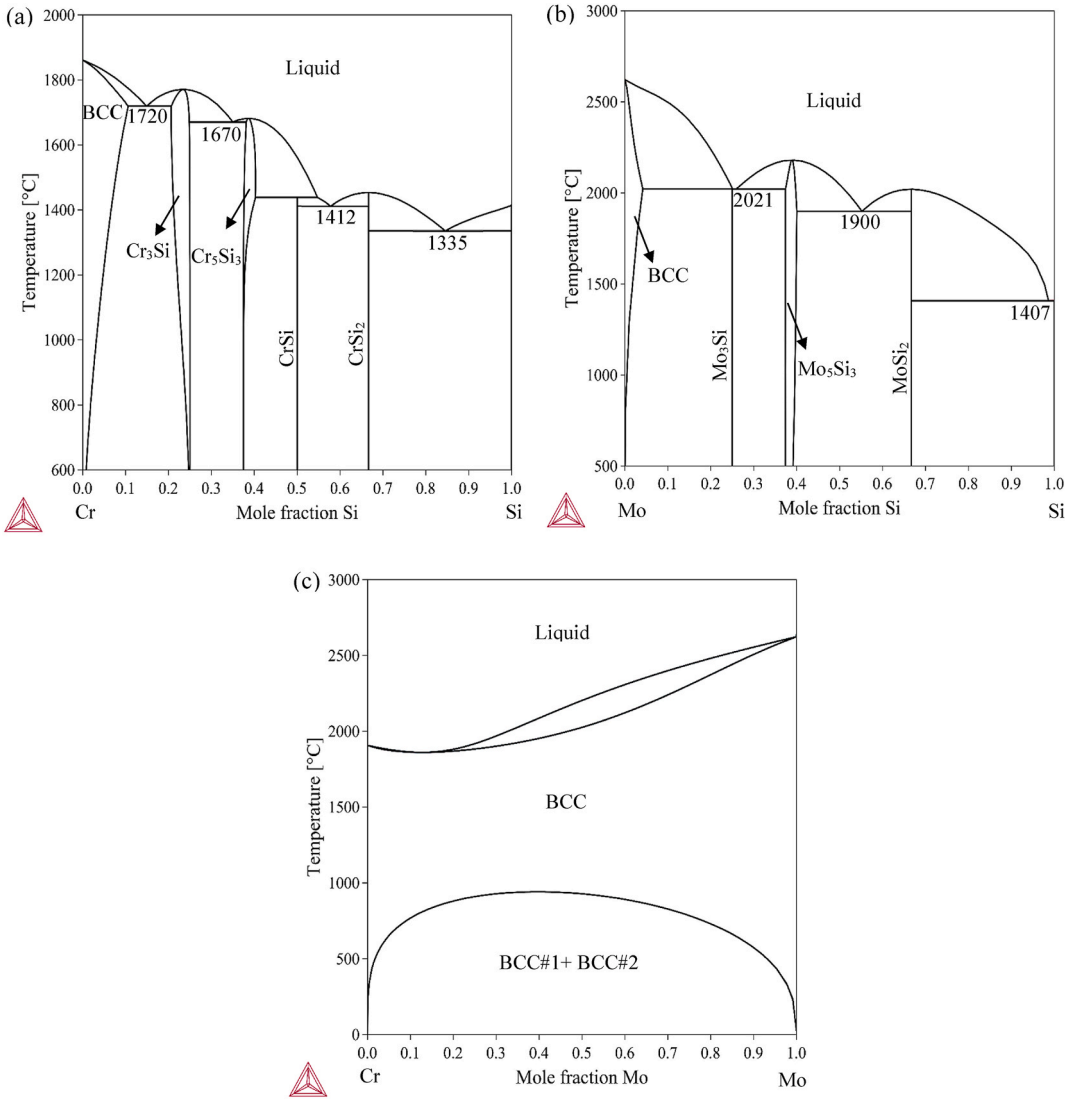


Fig. 1. Calculated binary phase diagrams: (a) Cr-Si [29], (b) Mo-Si [30] and (c) Cr-Mo [31].

1200 and 1600 °C and re-optimized the phase diagram using Calculation of Phase Diagram (CALPHAD) approach by incorporating the melting point of Cr as 1861 ± 3 °C, and a considerable solubility range for Cr_5Si_3 phase. Their DTA measurements confirmed the absence of β-Cr_5Si_3. In the present work, the Cr-Si phase diagram is calculated based on the thermodynamic description adapted from Ref. [29] (Fig. 1a).

2.2. Mo-Si system

The earliest extensive study of the Mo-Si binary system performed by Kieffer and Cerwenka [32] using XRD, melting point measurements using pyrometer and microstructural analysis for a complete composition range. This [32] study identified three intermetallic phases – Mo_3Si, Mo_3Si_2 and $MoSi_2$ – along with terminal solid solutions. Svechnikov et al. [33] provided a reliable Mo-Si phase diagram including invariant reactions, liquidus and solidus temperatures based on own XRD, and high temperature DTA measurements. However, the phase previously identified as Mo_3Si_2 was reclassified to Mo_5Si_3 with a homogeneity range of 36.5 – 39.0 at. % Si [33]. A polymorphic phase transformation of the $MoSi_2$ phase at 1900 °C from a low-temperature tetragonal (α-$MoSi_2$) C11b to a high temperature hexagonal (β-$MoSi_2$) C40 structure was reported in Refs. [33–35]. However, Frankwicz and Perepezko [36] confirmed that β-$MoSi_2$ is metastable. In a recent study, Czerny et al. [37] have reported a deficiency of 23 at. % Si-content within Mo_3Si phase, which is in agreement with earlier findings [38,39]. Based on this observation, the authors [37] re-optimized the Mo-Si phase diagram, taking into account the heat capacity data from Ref. [40]. The present work accepts the thermodynamic description from Ref. [30] to calculate the Mo-Si phase diagram (Fig. 1b).

2.3. Cr-Mo system

Comparing to Cr-Si and Mo-Si systems, the Cr-Mo system is relatively simple without any intermetallic phases. This binary system is composed of liquid phase and (Cr,Mo)ss with a miscibility gap. The critical temperature of the miscibility gap is between 900 °C and 950 °C as reported in Kubaschewski and Chart [41]. A thermodynamic assessment of the Cr–Mo binary conducted by Frisk and Gustafson [31] is adopted in the present work (Fig. 1c).

2.4. Cr-Mo-Si system

Although the binary phase relations in Mo-Si, Cr-Si, and Mo-Cr systems are relatively well established, the Cr-Mo-Si ternary system remains less comprehensively understood. The concurrent presence of BCC solid solutions and intermetallic silicides introduces complex thermodynamic and kinetic interactions that strongly influence microstructure and alloy properties. This complexity is particularly pronounced in the compositional region surrounding the σ phase, where phase boundaries are not yet fully resolved.

In [20], the authors calculated the energy required for stabilization of the σ-phase at 1500 °C to be approximately 2500 cal/gatom of metal. This value surpasses the simple binary interaction which implies that the phase's stability is not due to conventional Cr-Si or Mo-Si binary interactions but is instead driven by a specific ternary interaction parameter.

Mittel et al., [42] reported the formation of a C14 Laves phase with a hexagonal structure (hP12, $MgZn_2$ type). The Laves phase, which was observed in one sample composition of CrMoSi, coexisted with a (Cr,Mo) ss phase, along with an unidentified third phase. It is noteworthy that the C14 phase has not been reported in any of the binary systems (Mo−Cr, Mo−Si, or Cr−Si). Since the C14 phase is absent in all corresponding binary systems, its classification as a stable ternary phase cannot be supported based on such limited evidence. Furthermore, only two phases (Cr,Mo)ss and an unidentified phase were found in a second sample with the nominal composition Cr_3Mo_2Si that was synthesized under the same conditions, indicating the continuing presence of unreacted initial elements and incomplete equilibration. Pandelaers and Schmid-Fetzer [19] reported a comprehensive evaluation of the Cr-Mo-Si ternary system, focusing on phase equilibria, phase compositions, and crystallographic parameters. This article specifically describes quasibinary sections such as Mo_5Si_3 − Cr_5Si_3, $MoSi_2$ − $CrSi_2$, and Mo_3Si − Cr_3Si. It also provides data on homogeneity ranges and lattice parameters for various phases. Additionally, the authors constructed the isothermal section in the partial system Cr−CrMo−$MoSi_2$−$CrSi_2$ at 1300 °C, primarily based on the work of [21]. Hinrichs et al., [17] reported metastable σ-phase formation during arc melting for the alloy composition of Cr-13.5Si-32.2Mo (at.%) which decomposes into a fine lamellar microstructure of (Cr,Mo)ss and $(Cr,Mo)_3Si$ at 1200 °C. Rudy and Nowotny [20] reported the existence of the ternary σ-phase within a homogeneity range from $Cr_{28}Mo_{58}Si_{14}$ to $Cr_{49}Mo_{37}Si_{14}$ based on XRD analysis of fifteen arc melted samples heat treated at 1500 °C for 24 h and additionally at 1170 °C for 189 h. At 1170 °C the σ-phase undergoes an eutectoid decomposition into (Cr,Mo) + $(Cr,Mo)_3Si$.

In the liquidus projection reported in Ref. [22], nine primary solidification fields were identified, corresponding to phases such as BCC, M_3Si, $Mo(Cr)_5Si_3$, $Cr(Mo)_5Si_3$, $Mo(Cr)Si_2$, $Cr(Mo)Si_2$, Cr(Mo)Si, α-Cr $(Mo)_5Si_3$, and diamond-Si. The authors [22] identified six univariant reactions (four transitional eutectics and two peritectics). Notably, the stoichiometric compounds Mo_5Si_3 and α-Cr_5Si_3 have the same W_5Si_3-type structure but form different Mo-rich and Cr-rich solid solutions, separated by a miscibility gap. Solidification pathways were also determined in this work by examining primary and secondary phases in as-cast microstructures, observing both eutectic and peritectic morphologies, and mapping them onto the liquidus projection. The crystallographic data for the solid phases in Cr-Mo-Si ternary system are summarized in Table 1.

3. Experimental methods

To experimentally establish the phase equilibrium relations in Si-lean (<25 at.% Si) alloys within the Cr-Mo-Si ternary system, twelve ternary alloys were chosen (see Table 2). These alloys were systematically selected to construct the partial isothermal section, which includes compositions near binary boundaries and regions around the σ-phase. The alloys were prepared using Cr granules (99.94+% purity, Chempur), Mo pellets (99.98% purity, Chempur) and Si granules (99.999% purity, Chempur). The pure metals were melted in a vacuum arc melter in an argon atmosphere (99.9999% purity) using a non-consumable tungsten electrode with a water-cooled copper hearth. Prior to arc-melting, pure zirconium was melted to absorb residual oxygen in the chamber. The ingots with approximate mass of 50 g were remelted six times being flipped after each melting step to ensure compositional homogeneity. The mass loss of the specimens after melting was less than 1 wt%. The ingots were cut into pieces for analysis by using electrical discharge machining (EDM, ARTA 423 PRO). Heat treatment was carried out in a water cooled (Nabertherm, Germany) tube furnace under an argon protective atmosphere. The samples were wrapped in molybdenum (Mo) foils and placed in alumina (Al_2O_3) crucibles to prevent interaction with the furnace tube; Ti sponges were used to absorb residual oxygen. Heat treatment was carried out at 1500 °C for 200 h, followed by controlled furnace cooling at a rate of 150 °C/h.

The microstructure was analyzed by scanning electron microscopy (SEM) (Zeiss, MERLIN, SEM-BSE equipped with EDX) in back-scatter electron (BSE) mode with accelerating voltage of 20 kV and current of 5 nA. The equilibrium composition of each phase in alloys was measured by electron probe microanalyzer (EPMA, Cameca SX100, France), and the accelerating voltage and probe current are 15 kV and 20 nA, respectively. The samples for SEM examination were prepared by embedding (electroconductive hot mounting powder, DUROPLAST black), grinding (SiC paper) and polishing with diamond suspensions up to 1 μm followed by a colloidal silica suspension down to 0.1 μm,

Table 1
Crystallographic data of solid phases in Cr-Mo-Si.

Phase	Crystal Structure	Pearson symbol	prototype	Space group	Lattice parameters (nm)			References
					a	b	c	
Cr	Cubic	cI2	W	Im-3m	0.2910	-	-	[43]
Mo	Cubic	cI2	W	Im-3m	0.3147			[34,44]
Si	Cubic (Diamond)	cF8	Diamond	Fd-3m	0.5430			[45]
Cr_3Si	Cubic	cP8	Cr_3Si	Pm-3n	0.4558	-	-	[24,46]
Cr_5Si_3	Tetragonal	tI38	W_5Si_3	I4/mcm	0.9170	0.4636	-	[28]
CrSi	Cubic	cP8	FeSi	$P2_13$	0.4620	-	-	[47]
$CrSi_2$	Hexagonal	hP9	$CrSi_2$	$P6_422$	0.4428	-	0.6368	[48]
Mo_3Si	Cubic	cP8	Cr_3Si	Pm-3n	0.4890	-	-	[34,44]
Mo_5Si_3	Tetragonal	tI32	W_5Si_3	I4/mcm	0.9648	-	0.4910	[34,44]
$MoSi_2$	Tetragonal	tI6	$MoSi_2$	I4/mmm	0.3202	-	0.7843	[34,44]
σ	Tetragonal	tP30	CrFe	$P4_2$/mmm	0.9220	-	0.4810	[20]
					0.917 ± 0.001		0.477 ± 0.001	This work[a]
$Cr_{47}Mo_9Si_{44}$								[21]

[a] As-cast condition.

Table 2
Equilibrium composition of the Cr-Mo-Si ternary system at 1500 °C for 200 h.

Sample	Nominal composition, at. %			Phase Analysis	Phase composition, at%, by EPMA		
	Cr	Mo	Si		Cr	Mo	Si
A1	64.5	18.5	17	(Cr,Mo)ss	75.6 ± 0.2	19.9 ± 0.1	4.5 ± 0.2
				$(Cr,Mo)_3Si$	62.0 ± 0.1	18.2 ± 0.2	19.8 ± 0.1
A2	20	60.2	19.8	(Cr,Mo)ss	19.8 ± 0.4	77.9 ± 0.4	2.3 ± 0.1
				$(Cr,Mo)_3Si$	21.5 ± 1.3	57.4 ± 1.6	21.1 ± 0.3
A3	44	42	14	$(Cr,Mo)_3Si$	41.4 ± 0.2	38.3 ± 0.2	20.3 ± 0.1
				σ	45.2 ± 0.3	41.8 ± 0.3	13.0 ± 0.1
A4	51	32	17	$(Cr,Mo)_3Si$	50.3 ± 0.1	29.6 ± 0.1	20.1 ± 0.1
				σ	52.3 ± 0.1	34.7 ± 0.2	13.0 ± 0.1
A5	50	40	10	(Cr,Mo)ss	51.5 ± 0.2	43.8 ± 0.4	4.7 ± 0.3
				σ	48.8 ± 0.2	38.5 ± 0.2	12.7 ± 0.2
A6	52.8	34.2	13	$(Cr,Mo)_3Si$	50.8 ± 0.4	29.1 ± 0.4	20.1 ± 0.2
				σ	52.4 ± 0.2	34.6 ± 0.2	13.0 ± 0.2
A7	42	38	20	$(Cr,Mo)_3Si$	42.1 ± 0.4	37.4 ± 0.4	20.5 ± 0.2
				σ	45.6 ± 0.2	40.9 ± 0.3	13.5 ± 0.3
A8	50	36	14	$(Cr,Mo)_3Si$	49.5 ± 0.3	29.9 ± 0.2	20.6 ± 0.2
				σ	51.3 ± 0.4	35.5 ± 0.2	13.2 ± 0.3
A9	57.7	37.3	5	(Cr,Mo)ss	58.5 ± 0.3	36.4 ± 0.2	5.1 ± 0.2
				σ	52.2 ± 0.3	35.2 ± 0.3	12.5 ± 0.1
A10	36	50	14	(Cr,Mo)ss	32.7 ± 0.5	64.3 ± 0.5	3.0 ± 0.2
				$(Cr,Mo)_3Si$	33.6 ± 0.2	45.7 ± 0.2	20.7 ± 0.1
				σ	39.2 ± 0.2	47.6 ± 0.2	13.2 ± 0.2
A11	59	26.8	14.2	$(Cr,Mo)_3Si$	56.2 ± 0.2	24.1 ± 0.2	19.7 ± 0.1
				σ	56.8 ± 0.3	30.6 ± 0.3	12.6 ± 0.1
				(Cr,Mo)ss	67.7 ± 0.3	27.2 ± 0.3	5.1 ± 0.1
A12	34.5	48.5	17	(Cr,Mo)ss	33.2 ± 0.2	63.9 ± 0.3	2.9 ± 0.2
				$(Cr,Mo)_3Si$	33.3 ± 0.5	46.4 ± 0.5	20.3 ± 0.1
				σ	38.7 ± 0.3	48.3 ± 0.4	13.0 ± 0.1

whereas EPMA samples were prepared following the same procedures without embedding. No etching was performed. Phase identification in the samples was examined using an Empyrean X-ray diffractometer (Malvern Panalytical GmbH), equipped with a PIXCEL3D Medipix3 1×1 detector. Measurements were conducted in Bragg–Brentano geometry using monochromatized CuKα_1 radiation from a copper cathode source. The diffraction data were collected over a 2θ range of 20°-100° with a step of 0.013°. The phases were identified by comparing the diffraction patters with the Inorganic crystal structure database (ICSD). The lattice parameters were calculated by averaging the values obtained from 10 to 14 diffraction peaks. The given uncertainties correspond to the standard deviation of the obtained data set. Quantitative volume fractions of the phases were calculated using ImageJ software.

4. Results and discussion

The results of the phase equilibria of 12 alloys which were equilibrated at 1500 °C for 200h are summarized in Table 2, while the corresponding lattice parameters and phase volume fractions are presented in Table 3. Since no etching was performed, interpretation was conducted analysing the compositional contrast and crystallographic data. BSE micrographs and corresponding XRD patterns for the alloys with two- and three-phase microstructures are presented in Figs. 2 and 3, respectively.

The BSE images of a Cr-rich alloy A1 (Fig. 2a) and Mo-rich alloy A2 (Fig. 2c) reveal a two-phase equilibrium (Cr,Mo)ss (light grey) + $(Cr,Mo)_3Si$ (dark grey) identified by the respective XRD patterns (Fig. 2b and 2d). According to EPMA, the maximum solubility of Si in (Cr,Mo)ss is found to be 4.5 at.% in A1 and 2.3 at.% – in A2. The volume fraction of (Cr,Mo)ss is 58.7% and 12% for A1 and A2, respectively.

Another series of two-phase alloys (A3 and A4) representing equilibrium between the σ phase (light grey) and $(Cr,Mo)_3Si$ (dark grey) is shown in Fig. 2e and g. The concentration of Si in the σ phase was measured as 13 at. % in both A3 and A4 alloys. Comparing the XRD patterns of alloys A3 and A4 as represented in Fig. 2f and h, respectively, the position and number of the diffraction peaks of phases in the alloys

Table 3
Calculated lattice parameters and phase volume fractions of the phases in the Cr–Mo–Si alloys equilibrated at 1500 °C.

Sample	Phase Analysis	Lattice parameter (nm)	Phase fraction (vol%)
A1	(Cr,Mo)ss	0.2961 ± 0.002	58.7
	$(Cr,Mo)_3Si$	0.4735 ± 0.006	41.3
A2	(Cr,Mo)ss	0.3007 ± 0.003	12.2
	$(Cr,Mo)_3Si$	0.4799 ± 0.002	87.8
A3	$(Cr,Mo)_3Si$	0.4768 ± 0.002	84.1
	σ	a = 0.9203 ± 0.002, c = 0.4798 ± 0.001	15.9
A4	$(Cr,Mo)_3Si$	0.4742 ± 0.003	54.4
	σ	a = 0.9190 ± 0.001, c = 0.4785 ± 0.001	45.6
A5	(Cr,Mo)ss	0.3020 ± 0.002	82.1
	σ	a = 0.9210 ± 0.002, c = 0.4801 ± 0.001	17.9
A6	$(Cr,Mo)_3Si$	0.4790 ± 0.002	5.3
	σ	a = 0.9185 ± 0.002, c = 0.4788 ± 0.001	94.7
A7	$(Cr,Mo)_3Si$	0.4758 ± 0.003	92.8
	σ	a = 0.9193 ± 0.001, c = 0.4796 ± 0.002	7.2
A8	$(Cr,Mo)_3Si$	0.4779 ± 0.004	27.8
	σ	a = 0.9179 ± 0.001, c = 0.4794 ± 0.003	72.2
A9	(Cr,Mo)ss	0.3004 ± 0.003	93.5
	σ	a = 0.9185 ± 0.001, c = 0.4787 ± 0.001	6.5
A10	(Cr,Mo)ss	0.3021 ± 0.002	13.2
	$(Cr,Mo)_3Si$	0.4791 ± 0.003	39.6
	σ	a = 0.9193 ± 0.005, c = 0.4792 ± 0.003	47.2
A11	$(Cr,Mo)_3Si$	0.4737 ± 0.005	62.5
	σ	a = 0.9199 ± 0.003, c = 0.4764 ± 0.002	22.3
	(Cr,Mo)ss	0.2991 ± 0.001	15.3
A12	(Cr,Mo)ss	0.3016 ± 0.001	13.5
	$(Cr,Mo)_3Si$	0.4788 ± 0.001	64.2
	σ	a = 0.9189 ± 0.004, c = 0.4794 ± 0.003	22.3

A3 and A4 are consistent but intensity differs owing to different contents of $(Cr,Mo)_3Si$ and σ. The variation in the diffraction peak intensity likely indicates difference in the volume fraction of the phases as well as the development of preferred crystallographic orientation during solidification. In the alloy A4, the volume fractions of $(Cr,Mo)_3Si$ and σ are 54.4% and 45.6%, respectively, whereas they are 15.9% and 84.1% in the alloy A3, indicating a higher fraction of σ in A3. Since the microstructures of alloys A3 and A6 as well as A4, A7 and A8 are similar, the BSE images and the respective XRD patterns of alloys A3 and A4 are demonstrated in Fig. 2.

A two-phase equilibrium was identified between the σ phase and (Cr,Mo)ss in alloy A5 as shown in Fig. 2i. It can be seen that the light grey σ phase is completely surrounded by dark grey (Cr,Mo)ss and the corresponding XRD pattern is given in Fig. 2j. The volume fractions of (Cr,Mo)ss and σ are 82.1% and 17.9%, respectively. The microstructure of the alloy A9 is not included, as it does not differ significantly from that of the Alloy A5.

The BSE images of alloys A10 and A11 are presented in Fig. 3a and c, respectively. The observed microstructure in Fig. 3a indicates that the alloy A10 exhibits three-phase equilibrium between (Cr,Mo)ss, $(Cr,Mo)_3Si$ and σ phases. The solid solution phase (Cr,Mo)ss (light grey) is surrounded by $(Cr,Mo)_3Si$ (darkest area) and the σ phase (dark grey). Fig. 3c represents the microstructure of the alloy A11 which demonstrates three-phase equilibrium between the dark grey (Cr,Mo)ss, the light grey σ and the darkest grey $(Cr,Mo)_3Si$. The phase constitution in alloys A10 and A11 were confirmed by XRD patterns, as shown in Fig. 3b and d, respectively. EPMA analyses confirm three compositionally distinct phase fields corresponding to the (Cr,Mo)ss, $(Cr,Mo)_3Si$, and σ phases. Therefore, the equilibrium between (Cr,Mo)ss, $(Cr,Mo)_3Si$ and σ phases is established in the Mo-rich region for the alloy A10 and in the Cr-rich region – for the alloy A11. The measured solubilities of Si in (Cr,Mo)ss for alloy A10 and A11 are 3.0 and 5.1 at. %, respectively. The volume fraction of alloys summarized as: 13.2% (Cr,Mo)ss, 39.6% (Cr,Mo)$_3$Si, and 47.2% σ phase in the alloy A10 and 15.3% (Cr,Mo)ss, 62.5% $(Cr,Mo)_3Si$, and 22.3% σ phase in the alloy A11. It is worth mentioning that the three phase (Cr,Mo)ss + $(Cr,Mo)_3Si$ + σ equilibrium in Alloy A10 was previously reported by Rudy and Nowotny [20] for the 36Cr50Mo14Si (at.%) composition. As the microstructures of the alloy A10 and alloy A12 are similar, only the microstructure of the Alloy A10 is presented in Fig. 3.

The microstructural examination using BSE mode reveals the distinct differences in the phase contrast, particularly for (Cr,Mo)ss and σ phases in alloys A10 and A11 as well as for σ phase in A5, A3 and A4 alloys. In theory, the contrast observed in the BSE mode is largely attributed to variations in the average atomic number ($\bar{Z}$) of the constituent phases, a phenomenon known as Z-contrast [49,50]. The brighter regions in the micrograph reflect phases with a higher average atomic number, while the darker sections represent constituents with lower average atomic numbers. In this work, no experiments were conducted to specifically address the phase contrast differences.

Considering all investigated alloys in Table 2 containing the σ phase, the present results indicate that the σ-phase exhibits a ternary compound with Si concentrations between 12.5 and 13.5 at. % and homogeneity ranges extending from 30.6 to 48.3 at.% and from 38.7 to 56.8 at.% for Mo and Cr, respectively. The calculated lattice parameters for the σ-phase are a = 9.17 ± 0.01 Å and c = 4.77 ± 0.01 Å which agree with the values reported in Ref. [20]. The homogeneity range of the σ-phase implies that there are two adjacent three-phase regions, (Cr,Mo)ss + (Cr,Mo)$_3$Si + σ connected by the continuous single-phase field of σ. The determined homogeneity range of σ and the concentration of Si exhibits a clear inconsistency comparing with results reported in Ref. [20], where σ has a Si concentration of 14 at. % and homogeneity ranges of 29 – 47 at. % and 39 – 57 at. % for Mo and Cr, respectively. Notably, the maximum Si content in the present work (13.5 at. %) is slightly lower than that reported in Ref. [20] (14 at. %) indicating a higher degree of Si-deficiency of the σ-phase. The observed discrepancy of the solubility and homogeneity range between the current work and [20] can be rationalized by the significant difference in the annealing time – 24 h [20] vs 200 h (this work) at 1500 °C assuming insufficient equilibration of the alloys investigated in Ref. [20]. Therefore, the σ-phase homogeneity range established in the present investigation can be considered more reliable. The σ-phase evolution in the Cr–Mo–Si ternary system based on the experimentally observed phase constitution is summarized in Table 4.

4.1. Isothermal section and phase equilibrium relations at 1500 °C

Based on the experimental data obtained, the partial isothermal section of the Si-lean Cr-Mo-Si ternary system at 1500 °C has been constructed (Fig. 4a). It consists of three single-phase regions, three two-phase regions and one three-phase region. Although similar two-phase equilibria between (Cr,Mo)ss and $(Cr,Mo)_3Si$ as well as three-phase equilibria between (Cr,Mo)ss, $(Cr,Mo)_3Si$ and σ exist in both the Cr-rich and Mo-rich regions in isothermal section, notable phase composition differences are identified. The enlarged area in the vicinity of the σ-phase is additionally shown in Fig. 4b due to its narrow Si homogeneity range. From the constructed isothermal section, it can be inferred that the phase relations in this compositional range are primarily controlled by the binary subsystems [29–31] except of the ternary σ-phase area. The (Cr,Mo)ss phase field is characterized by a single-phase (Cr,Mo)ss, which is consistent with a complete mutual solubility of Cr and Mo in the Cr–Mo binary system [31]. With increasing Si content, the stability of this single-phase field decreases and a

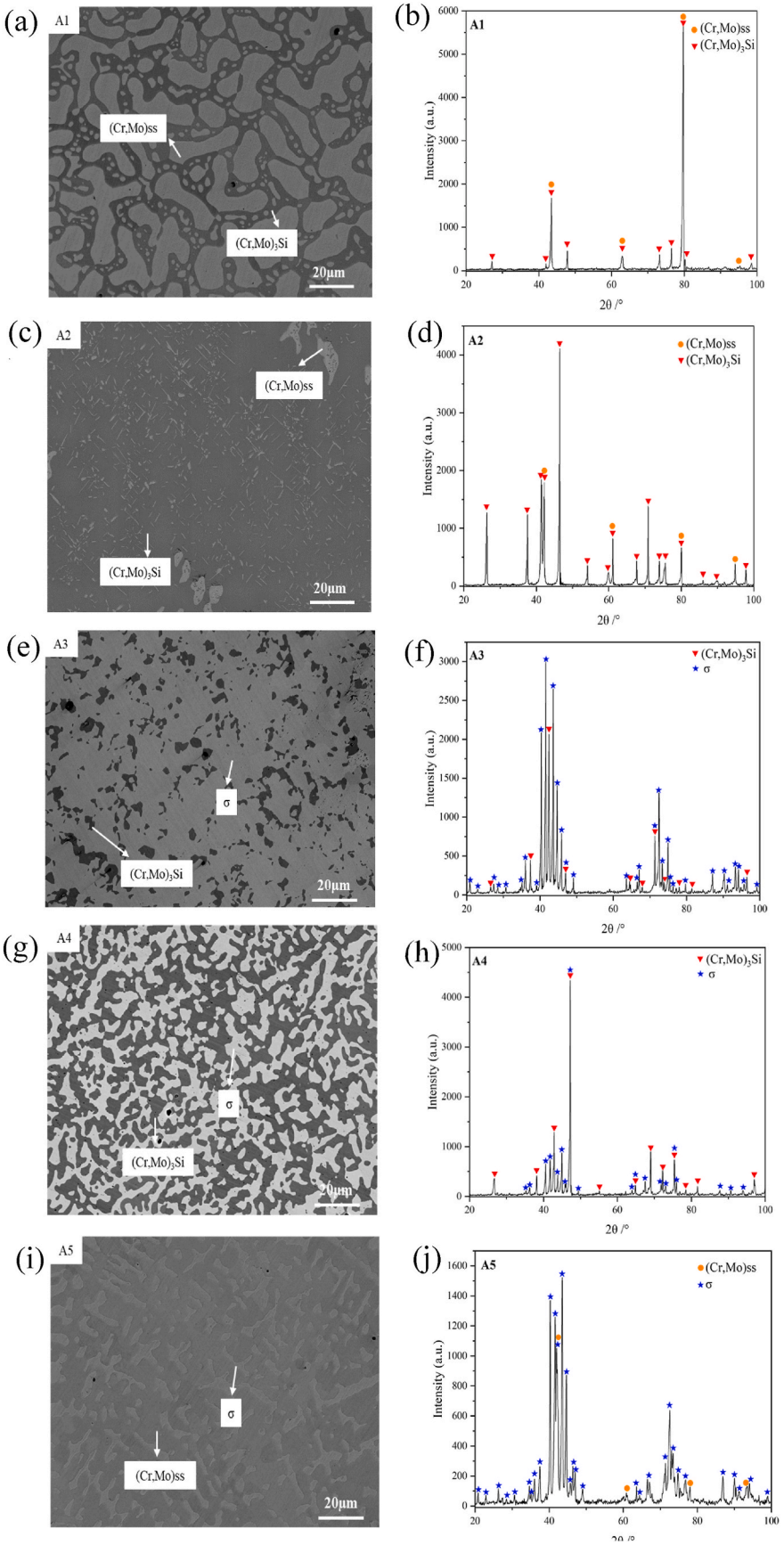


Fig. 2. BSE images and XRD patterns of the two-phase microstructure of the annealed samples at 1500 °C: (a) and (b) alloy A1; (c) and (d) alloy A2; (e) and (f) alloy A3; (g) and (h) alloy A4; (i) and (j) alloy A5.

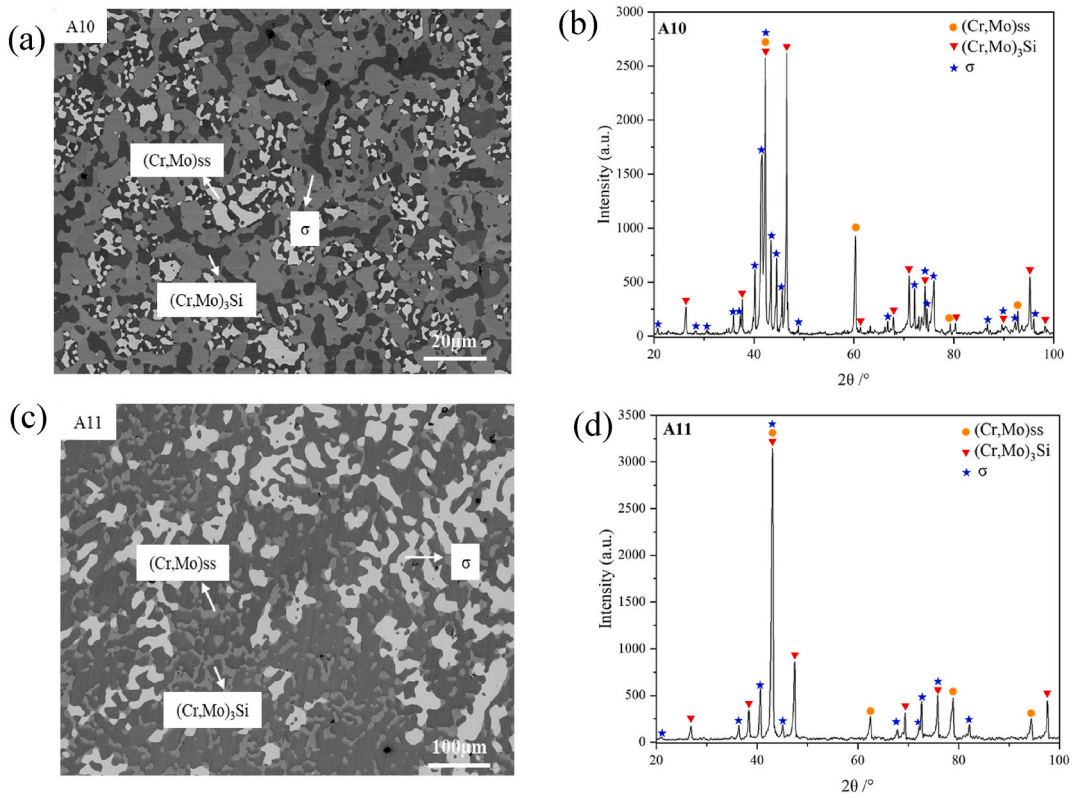


Fig. 3. BSE images and XRD patterns of the three-phase microstructure of the annealed samples at 1500 °C: (a) and (b) for alloy A10; (c) and (d) for alloy A11

Table 4
σ-Phase evolution in the Cr–Mo–Si ternary system.

Reference	Temperature	Experimental condition	σ-phase observation	Interpretation
Current work	1500 °C	200h annealing + controlled furnace cooling	σ-phase is stable within 12.5-13.5 at.% of Si, 30.6-48.3 at.% of Mo and 38.7-56.8 at. % of Cr	Equilibrium condition established experimentally based on compositional stabilization.
Rudy et al., [20]	1500 °C	Heat-treated/quenched Cr–Mo–Si alloys	σ phase reported, approximately Cr 39–57, Mo 29–47, Si ~14 at.%	Non-equilibrium σ reported
Koliotassis et al., [18]	1450 °C	20 h annealing + water quenching	σ observed in Cr–25Mo–8Si and Cr–40Mo–8Si	σ observed, but equilibrium not demonstrated
Koliotassis et al., [18]	1350 °C	100 h annealing + quenching	σ remained in Cr–40Mo–8Si	σ observed; equilibrium not independently established
Rudy et al., [20]	~1200 °C	Heat-treated/quenched Cr–Mo–Si alloys	σ undergoes eutectoid decomposition into $(Cr,Mo)_{ss}$ + $(Cr,Mo)_3Si$	Decomposition reported at approximately 1200 °C
Frauke et al., [17]	1200 °C	100 h annealing + furnace cooling	σ decomposes into $(Cr,Mo)_{ss}$ + $(Cr,Mo)_3Si$	Evidence of metastable σ decomposition

two-phase equilibrium between (Cr,Mo)ss and $(Cr,Mo)_3Si$ arises in the Mo- and Cr-rich sections of the phase diagram. Approaching the centre of the diagram, three-phase equilibria involving (Cr,Mo)ss, $(Cr,Mo)_3Si$, and the σ-phase appear. An intervening single-phase σ field connects these three-phase regions, reflecting the stability of the σ phase over a narrow but continuous composition range. By lowering the Si concentration, the equilibria change to 2 two-phase fields σ + (Cr,Mo)ss, while σ + $(Cr,Mo)_3Si$ region appears if Si content increases. At higher Si concentrations, the $(Cr,Mo)_3Si$ phase exhibits continuous solid solubility between Cr_3Si and Mo_3Si and is in equilibrium with the terminal (Cr,Mo) ss phase in the Mo- and Cr rich regions.

5. Conclusion

This study experimentally investigated the phase equilibria relations in the Cr-Mo-Si ternary system at 1500 °C using microstructural investigation (SEM/BSE), phase identification (XRD) and compositional determination (EPMA) methods. After 200 h annealing – established for the first time – the equilibrium condition is attained, a partial isothermal section is constructed, and a detailed characterization of the σ-phase is given.

The isothermal section of the Cr-Mo-Si ternary system in a Si deficient region ($x_{Si} \leq 25$ at.%) comprises three single-phase fields ((Cr,Mo) ss, $(Cr,Mo)_3Si$, σ), three two-phase fields ((Cr,Mo)ss + $(Cr,Mo)_3Si$ in both

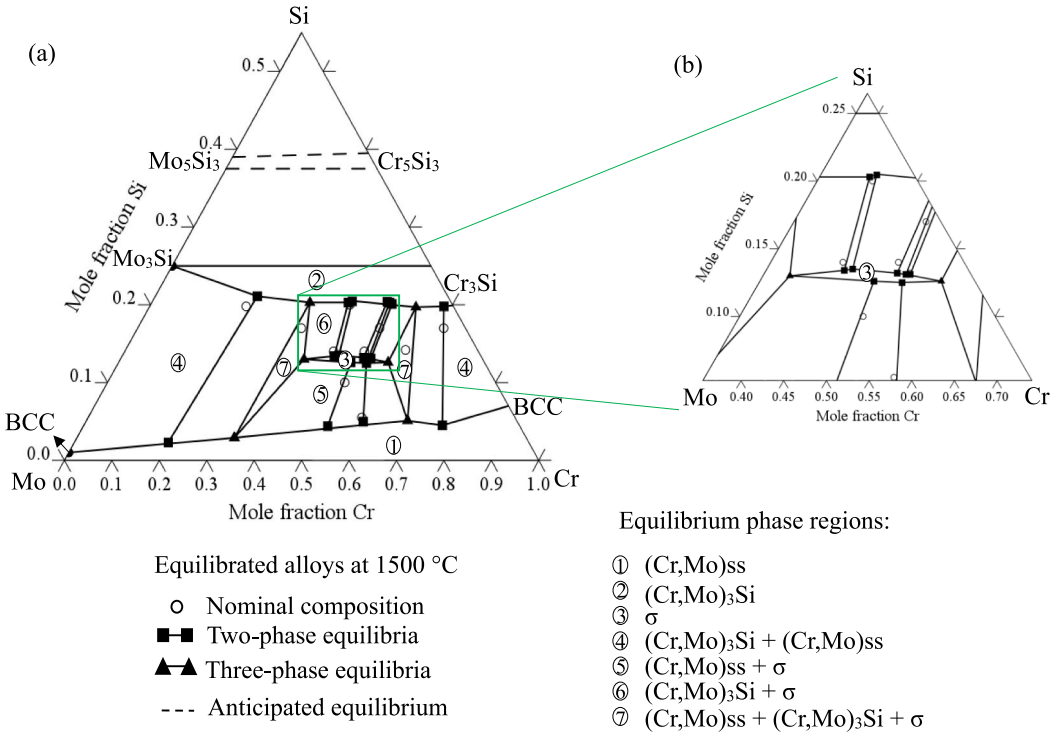


Fig. 4. a) Partially constructed isothermal section of Cr-Mo-Si ternary system at 1500 °C b) enlarged section of Fig. 4a to represent the single-phase σ at 1500 °C.

Cr-rich and Mo-rich domains, σ + (Cr,Mo)ss, and σ + $(Cr,Mo)_3Si$), and a single three-phase field (σ + (Cr,Mo)ss + $(Cr,Mo)_3Si$) that spans the Cr- and Mo-rich regions.

The σ-phase was unequivocally identified at 1500 °C. Its homogeneity range extends from 38.7 to 56.8 at. % and 30.6–48.3 at. % for Cr and Mo, respectively. The maximum Si solubility yielded a value of 13.5 at.%. The lattice parameters of the σ phase were determined from the XRD data and showed good agreement with the reported values.

CRediT authorship contribution statement

Arun Ramasamy Chitra: Writing – original draft, Visualization, Validation, Methodology, Investigation, Formal analysis, Data curation, Conceptualization. **Kateryna Khanchych:** Writing – review & editing. **Bronislava Gorr:** Writing – review & editing, Supervision, Project administration, Funding acquisition, Conceptualization.

Declaration of competing interest

The authors declare that they have no known competing financial interests or personal relationships that could have appeared to influence the work reported in this paper.

Acknowledgements

The authors thank Dr. Thomas Bergfeldt for ICP-OES measurements, Philip Kolja Erbes for EPMA measurements and Dr. Klaus Seeman for XRD measurements. This work has been financially supported by the German Research Foundation (DFG) as part of the Research Training Group 2561: Materials Compounds from Composite Materials for Applications in Extreme Conditions.

Appendix A. Supplementary data

Supplementary data to this article can be found online at https://doi.org/10.1016/j.calphad.2026.103016.

Data availability

Data will be made available on request.

References

[1] O.N. Senkov, P. Tsakiropoulos, J.P. Couzinié, Special issue "Advanced Refractory Alloys", Metals MDPI 12 (2022) 333.
[2] S.I. Jalali, M. Patullo, S. Park, C. Frey, K.M. Mullin, L.H. Mills, V. Kilic, C. Goodman, M. Foster, T.M. Pollock, K.J. Hemker, The thermal and mechanical response of refractory alloys at ultrahigh temperatures, Acta Mater. 304 (2026) 121781.
[3] L. Jiang, B. Zheng, C. Wu, P. Li, T. Xue, J. Wu, F. Han, Y. Chen, A review of Mo-Si intermetallic compounds as ultrahigh temperature material, Processes 10 (2022) 1772.
[4] J.H. Perepezko, The hotter the engine, the better, Science 326 (2009) 1068.
[5] M.J. Donachie, S.J. Donachie, Superalloys: a Technical Guide, ASM international, 2002.
[6] E. Lassner, W.D. Schubert, Tungsten: Properties, Chemistry, Technology of the Element, Alloys, and Chemical Compounds, Springer Science and Business Media, 2012.
[7] R.W. Cahn, P. Haasen, Physical Metallurgy, .1, Elsevier, 1996.
[8] L. Zhu, X. Wang, C. Mao, X. Ren, P. Feng, Influence of Ta_2O_5 on the micromorphology and high-temperature oxidation resistance of $MoSi_2$-based composite coating for protecting niobium, Mater. Charact. 179 (2021) 111328.
[9] J. Małecka, High-temperature oxidation of ti-al-nb alloys, Materials 15 (2022) 2137.
[10] Y. Zhang, K. Zhang, S. Lei, Y. Su, W. Yang, J. Wang, G. Qin, W. Li, Formation and oxidation behavior of TiO_2 modified Al_2O_3-Nb_2O_5/$NbAl_3$ composite coating prepared by two-step methods, Surf. Coating. Technol. 433 (2022) 128081.
[11] F. Hinrichs, G. Winkens, L.K. Kramer, G. Falcão, E.M. Hahn, D. Schliephake, M. K. Eusterholz, S. Sen, M.C. Galetz, H. Inui, A. Kauffmann, M. Heilmaier, A ductile chromium–molybdenum alloy resistant to high-temperature oxidation, Nature 646 (2025) 331–337.
[12] T. Guo, C. Dou, C. Wang, Z. Li, L. Zhang, H. Yu, D. Dong, C. Wang, K. Pan, High-temperature ablation behavior and microstructure evolution mechanism of W-4Re-0.27HfC alloy in plasma flame environment, Int. J. Refract. Metals Hard Mater. 133 (2025) 107375.
[13] T.M. Butler, O.N. Senkov, T.I. Daboiku, M.A. Velez, H.E. Schroader, L.G. Ware, M. S. Titus, Oxidation behaviors of CrNb, CrNbTi, and CrNbTaTi concentrated refractory alloys, Intermetallics 140 (2022) 107374.
[14] B. Gorr, J.H. Christ, High-temperature oxidation behaviour of Co-Re-Cr-based alloys: limitations and ways to improve, Adv. Mater. Res. 278 (2011) 545–550.
[15] L. Zander, M. Kerbstadt, E.M. White, M.C. Galetz, Cr-based high temperature alloys - the strengthening effect of molybdenum on chromium-silicon alloys, Int. J. Refract. Metals Hard Mater. 132 (2025) 107287.

[16] T.M. Butler, O.N. Senkov, M.A. Velez, T.I. Daboiku, Microstructures and mechanical properties of CrNb, CrNbTi, and CrNbTaTi concentrated refractory alloys, Intermetallics 138 (2021) 107323.
[17] F. Hinrichs, A. Kauffmann, A.S. Tirunilai, D. Schliephake, B. Beichert, G. Winkens, K. Beck, A.S. Ulrich, M.C. Galetz, Z. Long, H. Thota, Y. Eggeler, A. Pundt, M. Heilmaier, A novel nitridation- and pesting-resistant Cr-Si-Mo alloy, Corros. Sci. 207 (2022) 110566.
[18] L. Koliotassis, E.M. White, M.C. Galetz, The influence of Mo content and annealing on the oxidation behavior of Arc-Melted Cr–xMo–8Si alloys, Adv. Eng. Mater. 26 (2024) 2301906.
[19] L. Pandelaers, R. Schmid-Fetzer, Chromium – Molybdenum – Silicon, MSI Eureka, 2010, pp. 182–191.
[20] E. Rudy, H. Nowotny, A sigma-phase in the system cr-mo-si, Monatsh. Chem. 105 (1974) 156–168 (in German).
[21] V.N. Svechnikov, A. Kocherzhinskii, L.M. Yupko, Constitution and properties of the alloys of the mo-si-cr system, Sborn. Nauchn. Trudy Inst. Metallofiz. 20 (1964) 94–107 (in Russian).
[22] H. Wu, C. Li, C. Guo, Z. Du, Experimental determination of the isothermal sections and the liquidus surface projection of the Mo-Si-Cr ternary system, J. Alloys Compd. 922 (2022) 166164.
[23] H. Wu, C. Li, C. Guo, Z. Du, Thermodynamic assessment of the Cr–Mo–Si ternary system, Calphad 83 (2023) 102631.
[24] R. Kieffer, F. Benesovsky, H. Schroth, The system chromium-silicon and solid solutions of silicides, Z. Meteorol. 44 (1953) 437–442 (in German).
[25] H.J. Goldschmidt, J.A. Brand, The constitution of the chromium-niobium-silicon system, J. Less Common. Met. 3 (1961) 34–43.
[26] Y.A. Chang, Phase relationships in the system chromium-silicon, Trans. Metall. Soc. AIME 242 (1968) 1509–1515.
[27] V.N. Svechnikov, Y.A. Kocherzhinskii, L.M. Yupko, Chromium-silicon phase diagram, Sb. Nauchn. Rab. Inst. Metallofiz. Akad. Nauk. Ukr. SSR 19 (1964) 212–218 (in Russian).
[28] Y. Du, J.C. Schuster, Experimental reinvestigation of the CrSi-Si partial system and update of the thermodynamic description of the entire Cr–Si system, J. Phase Equil. 21 (2000) 281–286.
[29] K. Ioroi, I. Ohnuma, X. Xu, R. Kainuma, T. Omori, Thermodynamic assessment of the Cr–Si binary system, Calphad 85 (2024) 102690.
[30] C. Guo, C. Li, P.J. Masset, Z. Du, A thermodynamic description of the Al–Mo–Si system, Calphad 36 (2012) 100–109.
[31] K. Frisk, P. Gustafson, An assessment of the Cr-Mo-W system, Calphad 12 (1988) 247–254.
[32] R. Kieffer, E. Cerwenka, Beitrag zum system Molybdän-Silizium, Z. Metallke 43 (1952) 101.
[33] V.N. Svechnikov, Y.A. Kocherzhinskii, L.M. Yupko, Siagrammmy Sostoyaniya Metal Sist, Nauka, 1971, pp. 116–119.
[34] A.B. Gokhale, G.J. Abbaschian, The Mo-Si (Molybdenum-Silicon) system, J. Phase Equil. 12 (1991) 493–498.
[35] P.S. Frankwicz, J.H. Perepezko, Phase stability and solidification pathways in $MoSi_2$ based alloys, MRS Online Proc. Libr. 213 (1990) 169–174.
[36] P.S. Frankwicz, J.H. Perepezko, Phase stability of $MoSi_2$ in the $C11_b$ and C40 structures at high temperatures, Mater. Sci. Eng. A246 (1998) 199–206.
[37] A.K. Czerny, W. Ma, C.S. Hausner, P. Franke, M. Rohde, H.J. Seifert, Thermodynamic assessment of the Mo–Si system, Adv. Eng. Mater. 26 (2024) 2302085.
[38] I. Gnesin, B. Gnesin, Composition of the Mo-Mo_3Si alloys obtained via various methods, Int. J. Refract. Met. Hard Mater. 88 (2020) 105188.
[39] I. Rosales, J.H. Schneibel, Stoichiometry and mechanical properties of Mo_3Si, Intermetallics 8 (2000) 885–889.
[40] V.P. Bondarenko, E.N. Fomichev, A.A. Kalashnik, Heat transfer-sov, Res. 5 (1973) 76.
[41] O. Kubaschewski, T.G. Chart, Calculation of metallurgical equilibrium diagrams from thermochemical data, J. Inst. Met. 93 (1965) 329–338.
[42] R.C. Mittal, S.K. Si, K.P. Gupta, Si-stabilised Cl4 laves phases in the transition metal systems, J. Less Common. Met. 60 (1978) 75–82.
[43] R.G. Ross, W. Hume-Rothery, High temperature X-ray metallography, J. Less Common. Met. 5 (1963) 258–270.
[44] H. Okamoto, Mo-Si (molybdenum-silicon), J. Phase Equilibria Diffus. 32 (2011) 176.
[45] W.M. Yim, R.J. Paff, Thermal expansion of AlN, sapphire, and silicon, J. Appl. Phys. 45 (1974) 1456–1457.
[46] M. Jurisch, G. Behr, Growth and perfection of chromium-silicon (Cr_3Si) single crystals, Acta Phys. Acad. Sci. Hungar. 47 (1979) 201–207.
[47] B. Boren, X-ray study on alloys of silicon with chromium, manganese, cobalt and nickel, Arkiv. Kemi, Mineral. Geol. 11A (1933) 28.
[48] T. Dasgupta, J. Etourneau, B. Chevalier, S.F. Matar, A.M. Umarji, Structural, thermal and electrical properties of $CrSi_2$, J. Appl. Phys. 103 (2008) 113516.
[49] E.I. Suvorova, N.A. Arkharova, A.G. Ivanova, F.Y. Solomkin, P.A. Buffat, Phases and interfaces in the cr–fe–si ternary system: X-ray diffraction and electron microscopy study, Inorganics 11 (2023) 73.
[50] D.E. Newbury, N.W. Ritchie, Can x-ray spectrum imaging replace backscattered electrons for compositional contrast in the scanning electron microscope? Scanning 33 (2011) 174–192.